AGU ADVANCING EARTH AND SPACE SCIENCE

Geophysical Research Letters®

Key Points:

- We generated enhanced seismicity catalogs to investigate the potential link between sea level change and seismicity in a hydrothermal region
- Higher seismicity rates from the entire and declustered catalogs are observed during time periods when sea level is rising
- Strain estimates from local strainmeters show that seismicity was promoted during reduced normal and enhanced shear strain conditions

Sea Level Changes Affect Seismicity Rates in a Hydrothermal System Near Istanbul

P. Martínez-Garzón[1] [ID], **G. C. Beroza[2]** [ID], **G. M. Bocchini[3]** [ID], and **M. Bohnhoff[1,4]** [ID]

[1]Helmholtz Centre Potsdam GFZ German Research Centre for Geosciences, Section 4.2 Geomechanics and Scientific Drilling, Potsdam, Germany, [2]Department of Geophysics, Stanford University, Stanford, CA, USA, [3]Faculty of Geosciences, Institute of Geology, Mineralogy and Geophysics, Ruhr University Bochum, Bochum, Germany, [4]Institute of Geological Sciences, Free University Berlin, Berlin, Germany

Abstract Small stress changes such as those from sea level fluctuations can be large enough to trigger earthquakes. If small and large earthquakes initiate similarly, high-resolution catalogs with low detection thresholds are best suited to illuminate such processes. Below the Sea of Marmara section of the North Anatolian Fault, a segment of ≈150 km is late in its seismic cycle. We generated high-resolution seismicity catalogs for a hydrothermal region in the eastern Sea of Marmara employing AI-based and template matching techniques to investigate the link between sea level fluctuations and seismicity over 6 months. All high resolution catalogs show that local seismicity rates are larger during time periods shortly after local minima of sea level, when it is already rising. Local strainmeters indicate that seismicity is promoted when the ratio of differential to areal strain is the largest. The strain changes from sea level variations, on the order of 30–300 nstrain, are sufficient to promote seismicity.

Plain Language Summary Quasi-periodic phenomena are a natural probe to test how the Earth's responses to a certain stress perturbation. High-resolution catalogs with low detection thresholds may provide a new opportunity to look for this type of earthquake triggering. A segment of 150 km below the Sea of Marmara section of the North Anatolian Fault is late in its seismic cycle. Here, we generated high-resolution seismicity catalogs for 6 months covering a hydrothermal region south of Istanbul in the eastern Sea of Marmara including seismicity up to M_W 4.5. For first time in this region, we document a strong effect of the Sea of Marmara water level changes on the local seismicity. Both high-resolution catalogs show that local seismicity rates are significantly larger during time periods shortly after local minima on sea level, when the sea level is rising. The available local instrumentation provided an estimate of the strain changes that were sufficient to promote seismicity. If such small stress perturbations from sea level changes are enough to trigger seismicity, it may suggest that the region is very close to failure.

1. Introduction

For decades the Earth's periodic phenomena such as tidal movements or seasonal effects have been studied to investigate whether small, but predictable stress changes are sufficient to trigger regular or low-frequency earthquakes (Obara, 2002; Tanaka et al., 2002). The response to a known forcing can provide insight into the stress change needed to activate faults and hence the probable timing of earthquakes, and more generally to the processes promoting earthquake initiation. Solid-Earth tides can trigger both earthquakes and tectonic tremor. The conditions that promote tremor include elevated pore pressure and low effective normal stresses, and hence triggering of tectonic tremor by solid-earth tides has been observed often where ambient tremor occurs, including Nankai (Shelly et al., 2007), Cascadia (Rubinstein et al., 2008), and the creeping portion of the San Andreas Fault (Thomas et al., 2009, van der Elst et al., 2016). Tidal triggering of earthquakes is far less common, and has been observed in only a few places where the Earth's crust is sufficiently close to failure that small stress changes can induce slip, including shallow thrust faults at global scale (Cochran et al., 2004) and mid-oceanic ridges such as the East Pacific Rise (Stroup et al., 2007). An extreme case of triggered seismicity from periodic changes in the water level comes from the Koyna and Warna hydro-electric power plants in India, where $M > 5$ earthquakes have occurred following water level increase from monsoon rains (Bansal et al., 2018; Gupta, 2018). Some models of earthquake nucleation hold that large and small earthquakes begin similarly (Beroza & Ellsworth, 1996; Ellsworth & Beroza, 1995). If small and large earthquakes share a common nucleation process, high-resolution earthquake catalogs should be useful to better illuminate it.

In the last few years, fast and efficient processing of vast data volumes has been achieved with the emergence and application of artificial intelligence (AI). AI methods are promising for addressing a number of seismological challenges, including enhancing seismicity catalogs (e.g., Zhu & Beroza, 2019) and open new opportunities for better capturing physical processes compared with traditional seismicity catalogs, such as the detailed imaging of fault architecture (Ross et al., 2019) and elucidation of pathways between fluid-injection wells (Park et al., 2020). Such catalogs provide a new opportunity to investigate earthquake triggering; however, their properties warrant a thorough evaluation to minimize false detections and interpret the results with confidence. For that reason, it is essential to compare and benchmark results from AI-based seismic catalogs with those obtained with traditional catalogs and other well-established high-resolution techniques such as template matching.

The major plate bounding North Anatolian Fault in Türkiye splits into several segments before entering the Sea of Marmara, where it runs within 20 km of metropolitan Istanbul (Figure 1a). That 150-km fault segment last ruptured in a $M > 7$ earthquake in 1766, 256 years ago. Because the recurrence interval for $M > 7$ earthquakes is approximately 250 years (Parsons, 2004), the fault is considered to be late in its seismic cycle (Bohnhoff et al., 2013). The Armutlu Peninsula, on the southern shore of the Sea of Marmara, directly south of Istanbul, is a hydrothermal region displaying high heat flow and abundant hot springs (Eisenlohr, 1995). The area is rich in crustal fluids likely resulting in elevated pore pressures (Figure 1). Seismic swarms frequently occur, connected with episodic slow-slip transients (Martínez-Garzón et al., 2019, 2021). Hydrothermal regions are frequently observed to be sensitive to earthquake triggering, for example, following the occurrence of large local or regional earthquakes (Aiken & Peng, 2014; Saar & Manga, 2003). Similarly, the Armutlu Peninsula is sensitive to local stress perturbations from large earthquakes, hosting vigorous aftershock activity following the 1999 M_W 7.4 Izmit earthquake (Durand et al., 2010; Karabulut et al., 2011).

The northern portion of the Armutlu Peninsula (Figure 1) has been interpreted as a horsetail splay fault structure associated with a major normal fault (Kinscher et al., 2013) and it may have hosted the M 6.3 normal-faulting earthquake in 1963 (Bulut & Aktar, 2007; Pinar et al., 2003). The region also hosted the western termination of the 1999 M_W 7.4 İzmit earthquake rupture (Armijo et al., 2005). In recent years, the northern portion of the Armutlu Peninsula displays one of the highest background seismicity rates in the Sea of Marmara (Martínez-Garzón, Ben-Zion, et al., 2019; Wollin et al., 2018). Two slow-deformation transients, possibly related to the shallow part of local normal faults have been observed with strainmeter recordings to occur temporally connected with moderate $M > 4$ local seismic events (Martínez-Garzón et al., 2019, 2021).

We investigated the potential link between sea level changes and seismicity in the Armutlu peninsula over a time period of 6 months. This time period includes a complex earthquake sequence that took place in the northern portion of the Armutlu Peninsula, with two $M > 4$ seismic events. The largest event, a M_W 4.5 activated an onshore normal fault that hosted at least three periods of intense seismic activity over the following year (Bocchini, Martínez-Garzón, et al., 2022; Martínez-Garzón et al., 2021, see SMARTNET seismicity in Figure 1b). In this study, we generated enhanced seismicity catalogs using both AI-based and template-matching techniques, and compared the results with those from the standard catalogs. Both high-resolution catalogs show that local seismicity rates are larger during the time periods shortly after local minima in the sea level, when the sea level is rising. This correlation is not apparent in the standard seismicity catalogs. During that time, data from the local strainmeter BOZ1 indicates a minimum and maximum in the areal and differential strain, respectively, suggesting that stress conditions are optimal to trigger seismicity.

2. Data and Methods

We focused on a time window spanning 183 days from 1 November 2018 to 05 May 2019, in the northern Armutlu region (longitude 28.80–29.10, latitude 40.4–40.625) (Figure 1). The region hosted a vigorous seismic sequence, including a M_W 4.3 and a M_W 4.5 earthquakes rupturing a small normal fault. The analyzed time period includes the most seismically active period between January 2018 and 2020 (Figure 1b).

We analyzed time series from the tidal gauge stations YLVA and MERG, located in the Armutlu Peninsula and northern shore of the Sea of Marmara, respectively, and providing a measurement every 15 min (Figure S2 in Supporting Information S1). The long-term records (2018–2020) show a seasonality pattern in that from October to April, sea level displays larger and more rapid variations up to 0.8 m, while from April to September sea level changes are smaller than 0.3 m (Figures 1b and 1c). The variation of sea level in winter is typically
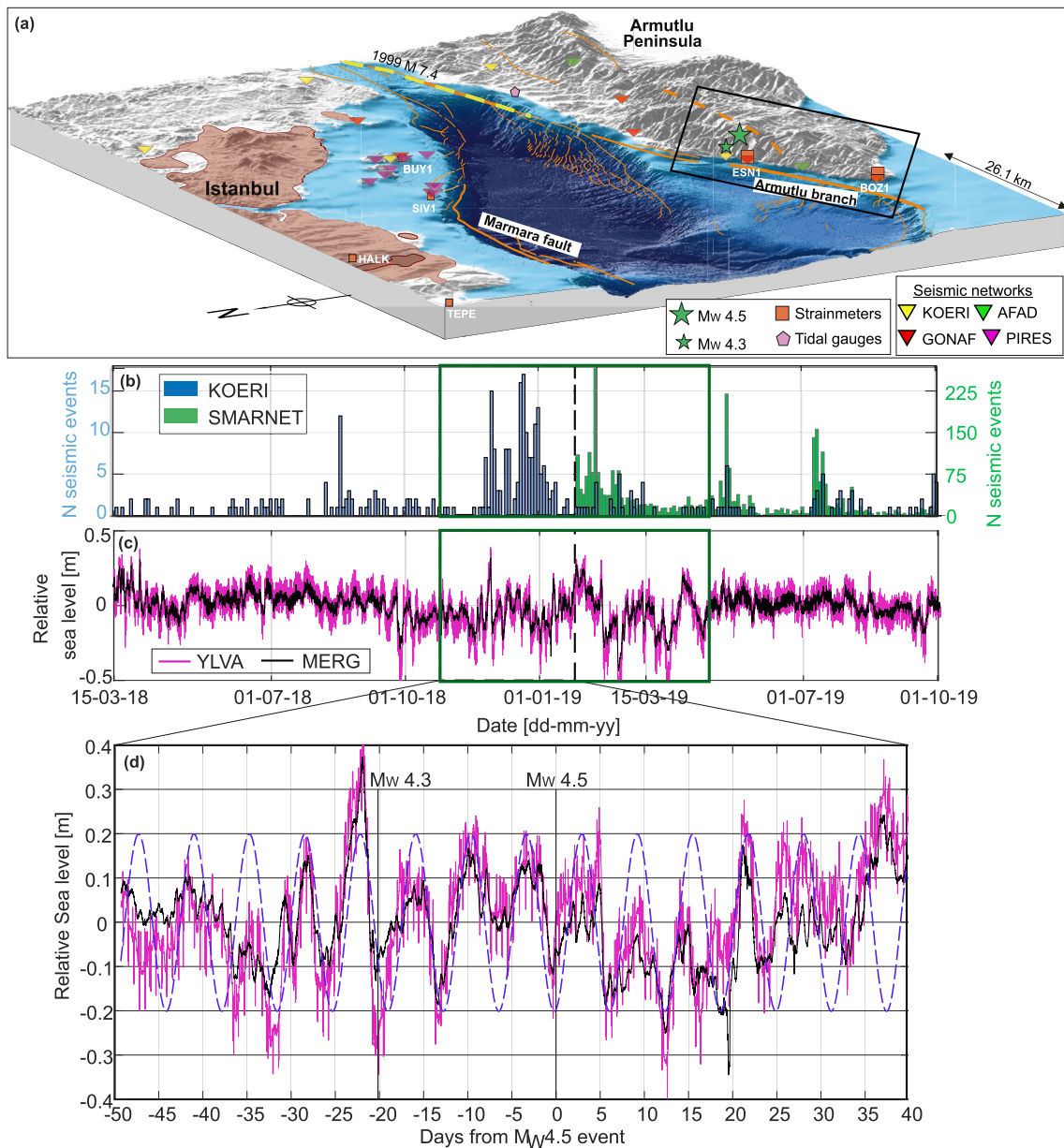
Figure 1. (a) Topography and bathymetry of the eastern Sea of Marmara region. Black rectangle frames the study area. (b) Seismicity rates from a standard catalog (KOERI agency and SMARTNET temporary network with blue and green bars, respectively) shown in two-day bins for northern Armutlu Peninsula. (c) Relative sea level changes from two tidal gauge stations located in Yalova and Ereglisi (magenta and black lines, respectively, see their location in Figure S2 in Supporting Information S1). In (b) and (c) the black dashed rectangle marks the time period for which we developed here enhanced seismicity catalogs. The solid rectangle frames the entire period analyzed. (d) Zoom of the relative sea-level changes during the time period for which we developed seismicity catalogs. Dashed blue line is a sinusoidal function with a period of $T = 6.3$ days.

up to three times larger than in summer, and it is typically linked with changes in the barometric pressure and wind forcing (Yüce & Alpar, 1997). For the time window between 1 November 2018 and 31 January 2019, we generated three enhanced seismicity catalogs employing AI-based and template-matching techniques and compared the results with those obtained with the standard catalogs. Venn diagrams (Figure S1 in Supporting Information S1) illustrate the common detections between the different datasets. The relatively low number of common events between the catalogs likely reflects that each of these catalogs is a biased representation of the "real catalog." The catalog derived with AI-based techniques is more effective in homogeneously sampling the entire spatio-temporal domain, while the template matching catalogs are more appropriate for analyzing

seismicity rates and small events coming from selected areas. In the following we describe the individual catalogs. In all catalogs, we assumed $M_L \approx M_W$ for earthquakes with $M_L < 4$ when no M_W was available (Kılıç et al., 2017).

1. Catalog derived utilizing AI-based techniques. We applied the PhaseNet deep learning method (Zhu & Beroza, 2019) to detect and pick the P-and S- waves of seismic events embedded in continuous seismic recordings from 16 stations surrounding the region of interest (Figure S2 in Supporting Information S1) resampled at 100 Hz. The method was trained on a data set from Northern California, but has been shown to generalize well to other tectonic settings. We obtained 323,085 picks, of which 166,963 (51%) are P-wave picks. The picks were associated into seismic events using the GaMMA association method (Zhu et al., 2022). We manually checked waveforms from all detections and 516 seismic events with visually clear waveforms were retained. We estimated their location using the non-linear earthquake location algorithm NLLoc (Lomax et al., 2000) and the velocity model from Bulut et al. (2009). The locations of the final 390 events for which five or more picks were available are provided in Figure S3 in Supporting Information S1. The catalog is available in Martínez-Garzón et al. (2023).

2. Template matching catalog A. We applied the matched filter algorithm EQcorrscan (Chamberlain et al., 2017) to the two closest seismic stations with the largest data recovery during the period of interest, ARMT and MDNY (Figure S2 in Supporting Information S1). Details on this catalog are included in Text S1 in Supporting Information S1. This catalog contains 2,462 seismic events (all manually reviewed) with magnitudes M_W in the range [−2.4, 4.5]. Because of the inclusion of only two stations, independent location of these events is not possible. The catalog is available in Martínez-Garzón et al. (2023).

3. Template matching catalog B. We derived a second template matching catalog utilizing 12 of the closest seismic stations displaying high seismic data recovery during the analyzed time period (Figure S2 in Supporting Information S1). An initial list of detections was generated following the same steps as for the Template Matching Catalog A, with the additional requirement that all detections must contain at least one pick from one of the two closest stations, ARMT and MDNY. All detections from this catalog were also manually reviewed. For events with more than five picks, we estimated their location using the non-linear algorithm NLLoc (Lomax et al., 2000) and the velocity model from Bulut et al. (2009). This catalog includes 717 seismic events with magnitudes M_W in the range [−2.1, 4.5] (Figure S4 in Supporting Information S1). The catalog is available in Martínez-Garzón et al. (2023).

To explore the relation between seismicity and sea level changes in the remaining three-month time period, we utilized an enhanced seismicity catalog for this region derived from a temporary seismic deployment in this area (SMARTNET network) containing up to 30 local stations (Bocchini et al., 2022a, 2022b; Martínez-Garzón et al., 2021; Figure 1b). We utilized both the entire catalog and a subset of it representing the background seismicity. The background events were identified using the nearest-neighbor approach of Zaliapin and Ben-Zion (2013).

The seismicity from these enhanced catalogs was compared with the following standard catalogs covering the entire analyzed period:

4. Turkish Disaster Management Presidency (AFAD) national seismicity catalog. For the selected time period and region, this catalog is composed of 144 seismic events with M_W in the range [0.9, 4.5].

5. KOERI national seismicity catalog. For the selected time period and region, this catalog is composed of 166 seismic events with M_W in the range 0.8–4.6.

The eastern Sea of Marmara region hosts six Gladwin tensor borehole strainmeters (150 m depth) at different locations deployed by UNAVCO (Figure 1a) and five of these were operating during the time period analyzed. The closest three to the M_W 4.5 earthquake are located at 5.5 km (ESN1), 22 km (BOZ1), and 32 km (BUY1). They are part of the Geophysical borehole Observatory at the North Anatolian Fault (GONAF, Bohnhoff et al., 2017; Figure 1a). Processing of strainmeter data is performed by UNAVCO and includes down-sampling from 300 to 1 sample per second to simplify data handling. Tidal corrections and borehole trends were applied to the strainmeter recordings following Hodgkinson et al. (2013). Corrections for the M2 (the largest lunar constituent) and O1 (lunar diurnal) tidal modes are calculated using the SPOTL (Agnew, 1996) tidal program and subtracted from each gauge. The correction of the borehole relaxation trend was calculated by fitting exponential functions to the raw data from the four different gauges of the strain tensor during the entire time of data
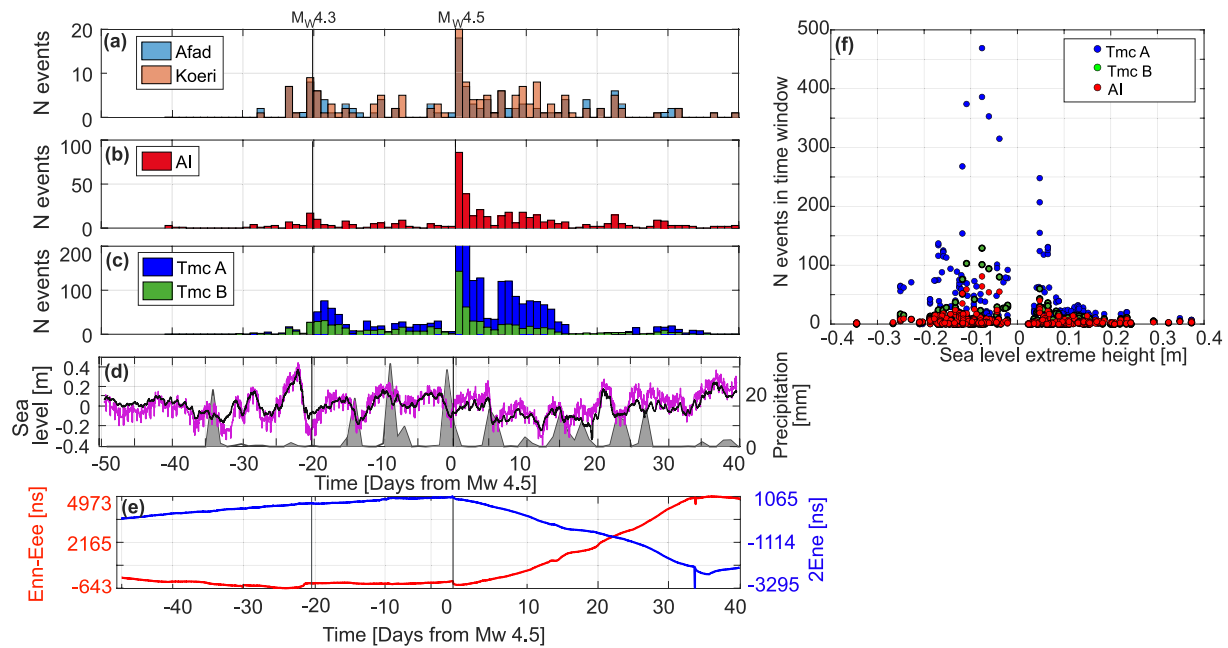
Figure 2. Evolution of daily seismicity rates for the seismicity catalogs and relation to the sea level, precipitation and slow slip during the first analyzed 90 days. (a) Seismicity rates from AFAD and KOERI catalogs, (b) Seismicity rates from the catalog derived with AI-based techniques, (c) Seismicity rates derived with two template matching catalogs utilizing different number of stations (see Data and Methods for details). (d) Sea level from the YLVA and MERG stations (magenta and black lines, respectively). Precipitation data from a pluviometric station in Yalova is represented with gray filled shapes. (e) Evolution of differential and engineering strain (red and blue lines, respectively) from BOZ1 strainmeter. A slow transient can be observed starting at day 0 (see Martínez-Garzón et al., 2021 for details). (f) Scatter plot displaying number of events in a time window of 6 hr as a function of the extreme sea level height on that window.

acquisition. From these corrected we calculated the areal ε_{N+E}, differential ε_{E-N} and engineering $2\varepsilon_{EN}$ strain components as:

$$\varepsilon_{N+E} = \varepsilon_{EE} + \varepsilon_{NN}$$

$$\varepsilon_{E-N} = \varepsilon_{EE} - \varepsilon_{NN} \tag{1}$$

$$2\varepsilon_{EN} = \varepsilon_{EN} + \varepsilon_{NE}$$

where ε_{EE}, ε_{NN}, and ε_{EN} are the three independent components of the horizontal strain tensor and the symmetry condition $\varepsilon_{EN} = \varepsilon_{NE}$ applies. We focus on the areal strain, ε_{N+E}, which is more sensitive to changes in the water column, as well as the differential strain, ε_{E-N}, which is more sensitive to tectonic deformation.

3. Results and Discussion

3.1. Seismicity Rates Modulated by Sea Level

The periodic functions best fitting the sea-level changes during the analyzed time period are a sinusoid with a period of $T = 6.3$ days until 30 January 2019 (Figure 1d) and a period of $T = 8.1$ days afterward. These two periods have been related to changes in the barometric pressure from wind forcing (Yüce & Alpar, 1997).

The amplitude of the sea-level change typically did not exceed ± 0.2 m, except on day -20 relative to the M_W 4.5 event, when seismicity rates increased including a M_W 4.3 earthquake shortly after a sea level decrease of -0.6 m, which was the largest sea-level change during the analyzed 6-month period (Figure 1c).

Both the M_W 4.3 and 4.5 earthquakes occurred shortly after local minima of the sea level (Figures 1d and 2). The five seismicity catalogs have very different magnitude detection thresholds, but the daily seismicity rates follow a similar distribution (Figure 2). Almost no seismic events were detected during the first 20 days (-50 to -30) in any of the catalogs. A small number of seismic events are present in the catalogs from day -28. Around day -20, after a local minimum in sea level the seismicity rates increased, including a M_W 4.3 event. Seismicity continued until day 0, culminating in the M_W 4.5 mainshock that ruptured the same onshore fault as the previous

M_W 4.3 event. Between days 0 and 16, seismicity rates were the highest in the observed period. Afterward, seismicity rates decayed, with only one more period of elevated seismicity after a local minimum of the sea level (day 25) (Figure 2). Plotting the daily seismicity rates as a function of the extreme sea-level height during that time period reveals that the three enhanced catalogs display a maximum in the seismicity rates when the sea level is −0.1 m (Figure 2f).

We investigated whether seismicity rates were affected by the phase of the sea level cycle. We assigned a phase of $\theta = 0, 360$ and $\theta = 180$ to each of the local sea level maxima and minima, respectively, so that phase values in the range [0–180] correspond to sea level decrease and values in the range [180–360] represent periods of sea level increase (Figure 3a, Figure S5 in Supporting Information S1). We evaluated the statistical significance of the observation of seismicity rates depending on sea level by applying a Schuster test (e.g., Cochran et al., 2004; Shelly et al., 2007) and defining a significance level of 1%. The null hypothesis is that the seismicity rates from the different catalogs are independent from the sea level phase. For the three enhanced catalogs combined with the SMARTNET catalog, the p-value rejects the null hypothesis at the defined significance level. This does not hold when using the two standard catalogs. Therefore, high-resolution catalogs strongly support the notion that the events from the entire catalog are not independent of sea level changes. Assigning the phase according to the sinusoid with period $T = 6.3$ days results in smoothing the sea-level variations, but the p-value remains smaller than significance level (Figure S6 in Supporting Information S1). The three high-resolution catalogs unambiguously show that seismicity rates are larger during the periods of sea-level increase, where the increase in the water body increases the stress loading (Figures 3b–3d). All three enhanced catalogs show a peak in the seismicity rates for $\theta \approx 200$, shortly after local minima, and a second peak around $\theta \approx 330$.

The selected time range included two earthquakes with magnitudes M_W 4.5 and 4.3 that generated their own aftershock sequences. We removed from the analysis all seismicity during two and one days following the M_W 4.5 and 4.3 mainshocks, respectively. These time ranges were selected based on the distribution of the number of events with respect to time following these mainshocks, which decayed to background level within those time periods (Figure S7 in Supporting Information S1). The mainshock M_W 4.5 triggered an aftershock sequence that can be fitted with an Omori law $N(t) = kt^{-p}$, with $p = 0.57$ and $k = 0.52$ (Figure S7c in Supporting Information S1). A $p < 1$ could indicate that the aftershock sequence from this event decayed slower than usual ($p \approx 1$). The aftershock sequence of the M_W 4.3 event is shorter and the Omori fit is worse (Figure S7d in Supporting Information S1). We also utilized a declustered version of the SMARTNET catalog (Bocchini et al., 2022a) to cover the remaining time period (Figure S8 in Supporting Information S1). Utilizing these catalogs of background seismicity, the p-values from the Schuster test still allow to reject the null hypothesis at the defined significance level, except with the AI-derived catalog. The peak of the distributions at $\theta \approx 200$ is considerably reduced (Figure 3).

Expanding the analysis to a longer continuous time period is difficult because between May and October 2019 the sea level displayed almost no long-term changes with amplitude >0.2 m. This suggests that a certain threshold normal stress change is needed for the sea-level changes to affect the seismicity rates.

A common source of periodicity in the seismicity rates is a difference between the day and night hours. Utilizing only the events included in our catalogs between 6p.m. and 9a.m. local time supports the observed dependencies, and hence they are not simply an artifact of different noise levels between day and night (Figure S9 in Supporting Information S1). The semi-diurnal tides are marginally observable in the tide-gauge time series (e.g., Figure 1d).

3.2. Constraining Strain Changes From Sea Level Movement

Strainmeters are sensitive to different tectonic, environmental and anthropogenic loading sources. Variations in the sea level are typically linked with changes in the barometric pressure, and mainly modify the vertical strain. The areal strain component ε_{N+E} is the most sensitive to vertical strain changes, and as such it is the one that most resembles the evolution of the sea level (Figure 4a, Figure S10 in Supporting Information S1). Between days −25 and −20 (containing the largest sea-level change immediately before the M_W 4.3 earthquake), we observe a change in ε_{N+E} of about −100, −700, and −100 nstrain in ESN1, BOZ1, and BUY1, respectively (Figure 4a, Figure S5 in Supporting Information S1). During that time, the change in the sea level was about $\Delta z = 0.6$ m. Therefore, the pressure change from the change in the water column would be approximately $\Delta P = \rho g \Delta z = 16$ kPa. The geological units in which the ESN1 and BOZ1 strainmeters are deployed are amphibolites and serpentinites, respectively (Eisenlohr, 1995). Assuming a Young's modulus of $E = 60$ GPa for these rocks, we can estimate the
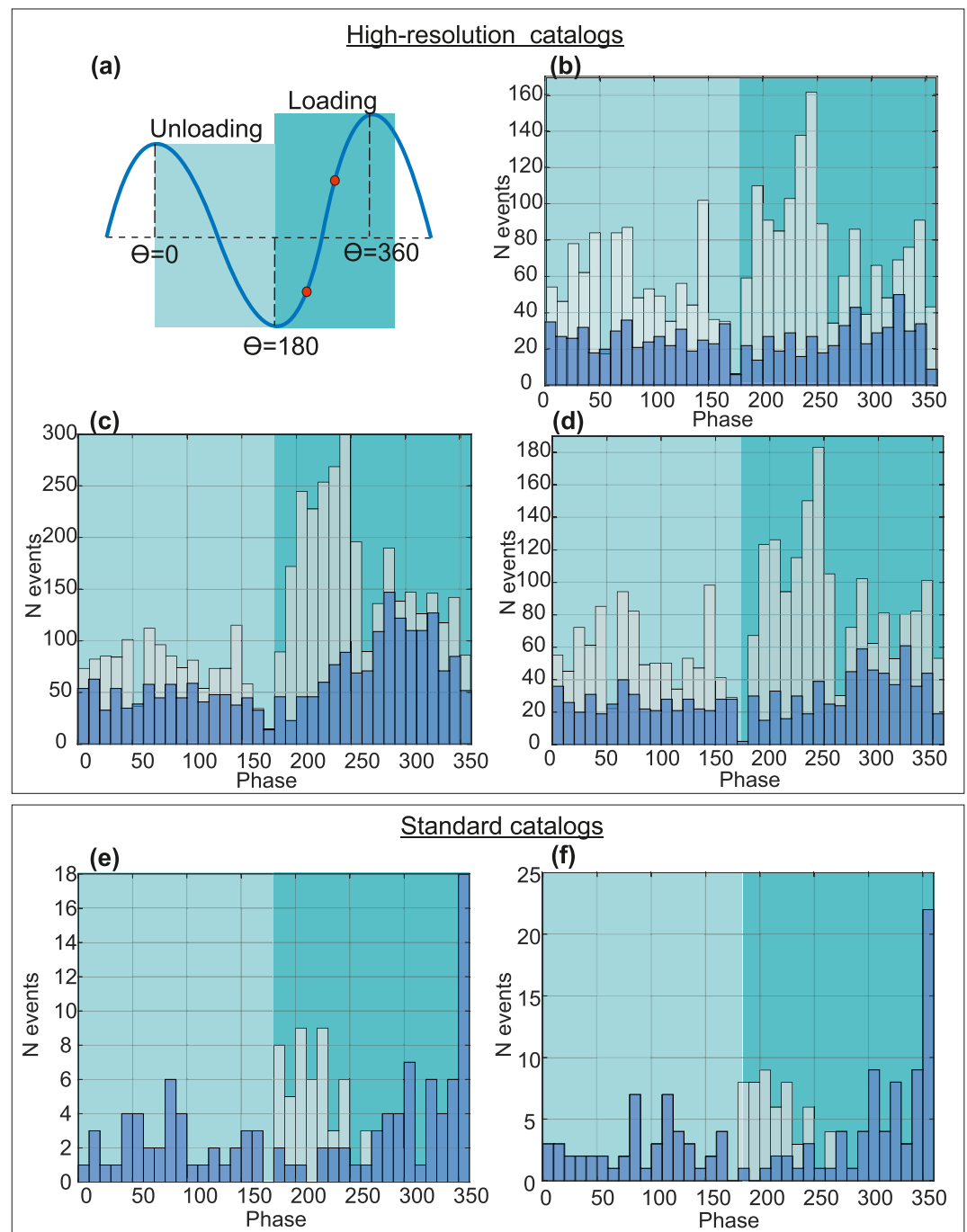
Figure 3. (a) Conceptual sketch illustrating the phases assigned to the observed sea level changes. Light and darker blue turquoise background colors differentiate the phases that represent a sea level increase and decrease, respectively. The two red circles illustrate approximately the tidal phases at which peaks of seismicity using the entire and declustered catalogs were observed, respectively. (b) Number of seismic events with respect of the sea level phase employing the seismicity catalog derived with AI techniques plus the SMARTNET catalog covering the analyzed time. (c, d) Same as (b) but for the template matching catalogs A and B. (e, f) Same as (b) but employing the standard seismicity catalogs from the national agencies AFAD and KOERI, respectively. In all plots, light gray bars represent the statistics utilizing the entire catalogs, while blue bars represent the background seismicity catalogs.

strain change from the change in the water column as $\Delta \in = \Delta P/E = 266\,\mathrm{nstrain}$, which is of the same order as observed (Figures 4a and 4b). The relation between the differential strain ε_{E-N} and the sea level is less obvious, because this component is more sensitive to shear strain changes, but some response is also observed during the
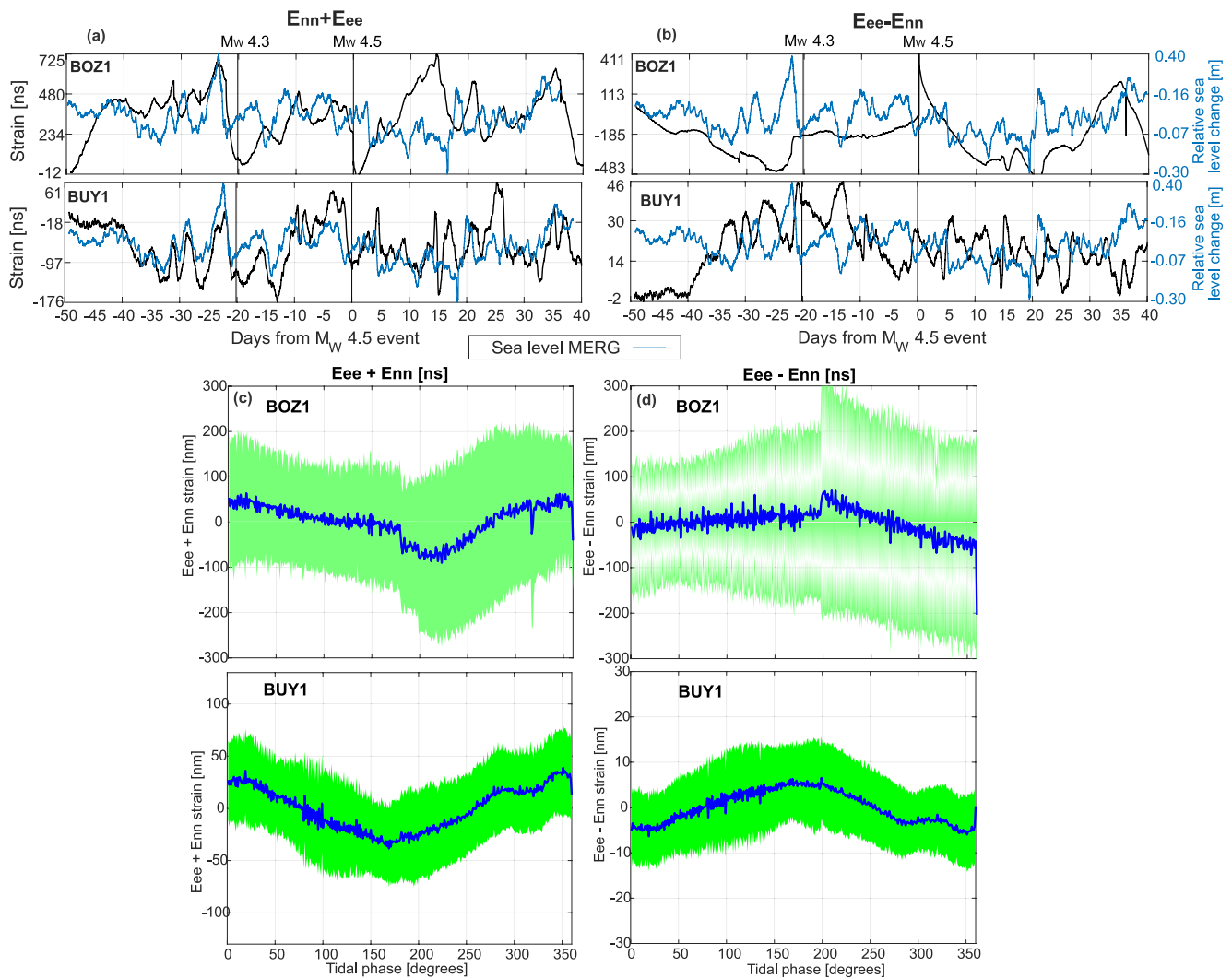
Figure 4. Evolution of (a) areal strainmeter components and (b) differential strain components during the analyzed time period for the strainmeters BOZ1 and BUY1 in the top and bottom panels, respectively (ordered from top to bottom according to distance to the M_W 4.5 event). Blue line represents the sea level evolution as recorded by MERG station (for units, see Figure 2). Vertical black lines mark the origin time of the M_W 4.3 and M_W 4.5 events that occurred within the study region. (c) Areal strain component from strainmeters BOZ1 and BUY1 with respect to tidal phase average over all cycles of the analyzed time period (blue line), together with its standard deviation (green area). (d) Same as (c) but for the differential strain component.

largest sea water changes (Figure 4b, Figure S10 in Supporting Information S1). The change in ε_{E-N} between the days −25 and −20 is approximately 60, 300, and 30 nstrain for ESN1, BOZ1, and BUY1, respectively. The differences in strain values recorded by the different strainmeters could be due to several local effects, including poroelastic effects, or the coupling between the instrument and the surrounding medium. This was well illustrated with the strong differences obtained between the modeled and observed coseismic strain offsets from the occurrence of several earthquakes in southern California (Barbour, 2015).

Estimating the average areal and differential strain components of the BOZ1 strainmeter over all tidal cycles shows that the areal ε_{N+E} (representing a normal strain) component reaches a minimum around $\theta = 180 - 200$, coinciding with the largest seismicity rates observed. Simultaneously, the differential component ε_{E-N} (representing a shear strain) reaches a maximum value (Figures 4c and 4d). We used only the BOZ1 strainmeter for this analysis, because the data from the other strainmeter in the area (ESN1) are incomplete during the analyzed time period. A similar cycle can be observed from the strainmeter BUY1, although this one is located further away from the study region and the strain changes appear smaller (Figures 4c and 4d). These observations are also in agreement with previous studies of earthquake triggering from tidal loading, where shallow thrust faults were

brought to slip when the Coulomb stress from the tidal movement was at its peak (Cochran et al., 2004). Reduced normal stress resulting in fault unclamping has also be observed to promote the occurrence of seismicity at The Geysers geothermal field (Delorey & Chen, 2022). However, we note that the standard deviation of the strain changes over the tidal cycle are large, and therefore the strain change is within the uncertainties of the strainmeter fluctuations. Recent experiments on laboratory rock samples subjected to periodic changes in the normal and shear stresses shown that rates of acoustic emissions were promoted during periods of pore pressure decrease (Chanard et al., 2019). As the faults that we observed to be seismically active during our analysis are mainly onshore, tracking the evolution of the pore pressure changes in the system with respect to tidal cycles is not trivial and therefore our observations cannot be directly compared.

4. Conclusions

We investigated the effect of stress variations from sea-level changes on the seismicity in a hydrothermal system in the eastern Sea of Marmara region in northwestern Türkiye over the course of 6 months. We generated high-resolution seismicity catalogs using both AI-based and template-matching techniques, and compared their results with standard catalogs employing traditional techniques. All enhanced catalogs showed that local seismicity rates from the catalogs significantly increased shortly after minima in the sea level, when the sea level is rising. This was not apparent in the standard catalogs. Recordings from nearby borehole strainmeters documented that during the sea-level phase $\theta = 200$, shortly after the minimum, the areal and differential strains reach minimum and maximum values, respectively, thus contributing to local fault unclamping and activation, although the standard deviation of the strain measurements is large and the strain change is within the associated uncertainties. The role of the sea-level changes in the seismicity rates supports the notion that the region is close to failure, and that small stress perturbations were able to trigger seismicity.

Data Availability Statement

Seismicity catalogs generated in this study with Artificial intelligence and template matching techniques are publicly available in the GFZ Data Service publication Martínez-Garzón et al. (2023). Seismicity catalogs from AFAD and KOERI agencies are available under the landing websites https://tdvms.afad.gov.tr/ (last accessed 05/08/2022) and http://www.koeri.boun.edu.tr/sismo/2/earthquake-catalog/ (last accessed 05/08/2022), respectively. The here generated AFAD and KOERI catalogs correspond to the time period from 1 November 2018 to 31 January 2019, and longitude and latitude ranges of 28.80°–29.10°, and 40.4°–40.625°, respectively. Data from the strainmeters (https://www.unavco.org/data/strain-seismic/bsm-data/bsm-data.html) are based on services provided by the Geodetic Facility for the Advancement of Geoscience (GAGE) Facility, operated by UNAVCO, Inc., with support from the National Science Foundation (NSF) and the National Aeronautics and Space Administration (NASA) under NSF Cooperative Agreement EAR-1724794. The here employed strainmeter time series correspond to instruments BOZ1, BUY1, ESN1, HALK, SIV1, and TEPE. For each of them, processed data in ASCII format is utilized.

References

Agnew, D. C. (1996). SPOTL: Some programs for ocean-tide loading. In *SIO reference series* (Vol. 96-8, p. 35). Scripps Institution of Oceanography.

Aiken, C., & Peng, Z. (2014). Dynamic triggering of microearthquakes in three geothermal/volcanic regions of California. *Journal of Geophysical Research: Solid Earth*, *119*(9), 6992–7009. https://doi.org/10.1002/2014JB011218

Armijo, R., Pondard, N., Meyer, B., Uçarkus, G., de Lépinay, B. M., Malavieille, J., et al. (2005). Submarine fault scarps in the Sea of Marmara pull-apart (North Anatolian Fault): Implications for seismic hazard in Istanbul. *Geochemistry, Geophysics, Geosystems*, *6*(6), Q06009. https://doi.org/10.1029/2004GC000896

Bansal, A. R., Rao, N. P., Peng, Z., Shashidhar, D., & Meng, X. (2018). Remote triggering in the Koyna-Warna reservoir-induced seismic zone, Western India. *Journal of Geophysical Research: Solid Earth*, *123*(3), 2318–2331. https://doi.org/10.1002/2017JB014563

Barbour, A. J. (2015). Pore pressure sensitivities to dynamic strains: Observations in active tectonic regions. *Journal of Geophysical Research: Solid Earth*, *120*(8), 5863–5883. https://doi.org/10.1002/2015JB012201

Beroza, G. C., & Ellsworth, W. L. (1996). Properties of the seismic nucleation phase. *Tectonophysics*, *261*(1), 209–227. https://doi.org/10.1016/0040-1951(96)00067-4

Bocchini, G. M., Martinez-Garzon, P., Verdecchia, A., Harrington, R., Bohnhoff, M., Turkmen, T., & Nurlu, M. (2022b). Enhanced seismicity catalog for the northern Armutlu Peninsula (northwestern Turkey) [Dataset]. GFZ Data Services. https://doi.org/10.5880/GFZ.4.2.2022.003

Bocchini, G. M., Martínez-Garzón, P., Verdecchia, A., Harrington, R. M., Bohnhoff, M., Turkmen, T., & Nurlu, M. (2022a). Direct evidence of a slow-slip transient modulating the spatiotemporal and frequency-magnitude earthquake distribution: Insights from the Armutlu Peninsula, Northwestern Turkey. *Geophysical Research Letters*, *49*(18), e2022GL099077. https://doi.org/10.1029/2022GL099077

Bohnhoff, M., Bulut, F., Dresen, G., Malin, P. E., Eken, T., & Aktar, M. (2013). An earthquake gap south of Istanbul. *Nature Communications*, *4*(1), 1999. https://doi.org/10.1038/ncomms2999

Bohnhoff, M., Dresen, G., Ceken, U., Kadirioglu, F. T., Kartal, R. F., Kilic, T., et al. (2017). GONAF-the borehole Geophysical Observatory at the North Anatolian Fault in the eastern Sea of Marmara. *Scientific Drilling*, *5*, 1–10. https://doi.org/10.5194/sd-22-19-2017

Bulut, F., & Aktar, M. (2007). Accurate relocation of İzmit earthquake (Mw = 7.4, 1999) aftershocks in Çınarcık Basin using double difference method. *Geophysical Research Letters*, *34*(10), L10307. https://doi.org/10.1029/2007GL029611

Bulut, F., Bohnhoff, M., Ellsworth, W. L., Aktar, M., & Dresen, G. (2009). Microseismicity at the North Anatolian Fault in the Sea of Marmara offshore Istanbul, NW Turkey. *Journal of Geophysical Research*, *114*(B9), B09302. https://doi.org/10.1029/2008JB006244

Chamberlain, C. J., Hopp, C. J., Boese, C. M., Warren-Smith, E., Chambers, D., Chu, S. X., et al. (2017). EQcorrscan: Repeating and near-repeating earthquake detection and analysis in Python. *Seismological Research Letters*, *89*(1), 173–181. https://doi.org/10.1785/0220170151

Chanard, K., Nicolas, A., Hatano, T., Petrelis, F., Latour, S., Vinciguerra, S., & Schubnel, A. (2019). Sensitivity of acoustic emission triggering to small pore pressure cycling perturbations during brittle creep. *Geophysical Research Letters*, *46*(13), 7414–7423. https://doi.org/10.1029/2019GL082093

Cochran, E. S., Vidale, J. E., & Tanaka, S. (2004). Earth Tides can trigger shallow thrust fault earthquakes. *Science*, *306*(5699), 1164–1166. https://doi.org/10.1126/science.1103961

Delorey, A. A., & Chen, T. (2022). Behavior of tidally triggered earthquakes depends on fluid conditions. *Bulletin of the Seismological Society of America*. https://doi.org/10.1785/0120220036

Durand, V., Bouchon, M., Karabulut, H., Marsan, D., Schmittbuhl, J., Bouin, M.-P., et al. (2010). Seismic interaction and delayed triggering along the North Anatolian Fault. *Geophysical Research Letters*, *37*(18). https://doi.org/10.1029/2010GL044688

Eisenlohr, T. (1995). Die Thermalwasser der Armutlu-Halbinsel (NW-Turkei) und deren Beziehung zu Geologie und aktiver Tektonik. ETH Zurich (PhD Thesis).

Ellsworth, W. L., & Beroza, G. C. (1995). Seismic evidence for an earthquake nucleation phase. *Science*, *268*(5212), 851–855. https://doi.org/10.1126/science.268.5212.851

Gupta, H. K. (2018). Review: Reservoir triggered seismicity (RTS) at Koyna, India, over the past 50 Yrs. *Bulletin of the Seismological Society of America*, *108*(5B), 2907–2918. https://doi.org/10.1785/0120180019

Hodgkinson, K., Langbein, J., Henderson, B., Mencin, D., & Borsa, A. (2013). Tidal calibration of plate boundary observatory borehole strainmeters. *Journal of Geophysical Research: Solid Earth*, *118*(1), 447–458. https://doi.org/10.1029/2012JB009651

Karabulut, H., Schmittbuhl, J., Özalaybey, S., Lengliné, O., Kömeç-Mutlu, A., Durand, V., et al. (2011). Evolution of the seismicity in the eastern Marmara Sea a decade before and after the 17 August 1999 Izmit earthquake. *Tectonophysics*, *510*(1–2), 17–27. https://doi.org/10.1016/j.tecto.2011.07.009

Kılıç, T., Ottemöller, L., Havskov, J., Yanık, K., Kılıçarslan, Ö., Alver, F., & Özyazıcıoğlu, M. (2017). Local magnitude scale for earthquakes in Turkey. *Journal of Seismology*, *21*(1), 35–46. https://doi.org/10.1007/s10950-016-9581-9

Kinscher, J., Krüger, F., Woith, H., Lühr, B. G., Hintersberger, E., Irmak, T. S., & Baris, S. (2013). Seismotectonics of the Armutlu peninsula (Marmara Sea, NW Turkey) from geological field observation and regional moment tensor inversion. *Tectonophysics*, *608*, 980–995. https://doi.org/10.1016/j.tecto.2013.07.016

Lomax, A., Virieux, J., Volant, P., & Berge-Thierry, C. (2000). Probabilistic earthquake location in 3D and layered models. In C. H. Thurber & N. Rabinowitz (Eds.), *Advances in seismic event location* (pp. 101–134). Kluwer. https://doi.org/10.1007/978-94-015-9536-0_5

Martínez-Garzón, P., Ben-Zion, Y., Zaliapin, I., & Bohnhoff, M. (2019). Seismic clustering in the Sea of Marmara: Implications for monitoring earthquake processes. *Tectonophysics*, *768*, 228176. https://doi.org/10.1016/j.tecto.2019.228176

Martínez-Garzón, P., Beroza, G. C., Bocchini, G. M., & Bohnhoff, M. (2023). *Earthquake catalogues from a hydrothermal system near Istanbul derived with template matching and AI techniques*. GFZ Data Services. https://doi.org/10.5880/GFZ.4.2.2023.001

Martínez-Garzón, P., Bohnhoff, M., Mencin, D., Kwiatek, G., Dresen, G., Hodgkinson, K., et al. (2019). Slow strain release along the eastern Marmara region offshore Istanbul in conjunction with enhanced local seismic moment release. *Earth and Planetary Science Letters*, *510*, 209–218. https://doi.org/10.1016/j.epsl.2019.01.001

Martínez-Garzón, P., Durand, V., Bentz, S., Kwiatek, G., Dresen, G., Turkmen, T., et al. (2021). Near-Fault Monitoring Reveals Combined Seismic and Slow Activation of a Fault Branch within the Istanbul–Marmara Seismic Gap in Northwest Turkey. *Seismological Research Letters*, *92*(6), 3743–3756. https://doi.org/10.1785/0220210047

Obara, K. (2002). Nonvolcanic deep tremor associated with subduction in southwest Japan. *Science*, *296*(5573), 1679–1681. https://doi.org/10.1126/science.1070378

Park, Y., Mousavi, S. M., Zhu, W., Ellsworth, W. L., & Beroza, G. C. (2020). Machine-learning-based analysis of the Guy-Greenbrier, Arkansas Earthquakes: A tale of two sequences. *Geophysical Research Letters*, *47*(6), e2020GL087032. https://doi.org/10.1029/2020GL087032

Parsons, T. (2004). Recalculated probability of M ≥ 7 earthquakes beneath the Sea of Marmara, Turkey. *Journal of Geophysical Research*, *109*(B5), B05304. https://doi.org/10.1029/2003JB002667

Pinar, A., Kuge, K., & Honkura, Y. (2003). Moment tensor inversion of recent small to moderate sized earthquakes: Implications for seismic hazard and active tectonics beneath the Sea of Marmara. *Geophysical Journal International*, *153*(1), 133–145. https://doi.org/10.1046/j.1365-246X.2003.01897.x

Ross, Z. E., Idini, B., Jia, Z., Stephenson, O. L., Zhong, M., Wang, X., et al. (2019). Hierarchical interlocked orthogonal faulting in the 2019 Ridgecrest earthquake sequence. *Science*, *366*, 346–351. https://doi.org/10.1126/science.aaz0109

Rubinstein, J. L., La Rocca, M., Vidale, J. E., Creager, K. C., & Wech, A. G. (2008). Tidal Modulation of Nonvolcanic Tremor. *Science*, *319*(5860), 186–189. https://doi.org/10.1126/science.1150558

Saar, M. O., & Manga, M. (2003). Seismicity induced by seasonal groundwater recharge at Mt. Hood, Oregon. *Earth and Planetary Science Letters*, *214*(3), 605–618. https://doi.org/10.1016/S0012-821X(03)00418-7

Shelly, D. R., Beroza, G. C., & Ide, S. (2007). Complex evolution of transient slip derived from precise tremor locations in Western Shikoku, Japan. *Geochemistry, Geophysics, Geosystems*, *8*(10). https://doi.org/10.1029/2007GC001640

Stroup, D. F., Bohnenstiehl, D. R., Tolstoy, M., Waldhauser, F., & Weekly, R. T. (2007). Pulse of the seafloor: Tidal triggering of microearthquakes at 9°50′N East Pacific Rise. *Geophysical Research Letters*, *34*(15). https://doi.org/10.1029/2007GL030088

Tanaka, S., Ohtake, M., & Sato, H. (2002). Evidence for tidal triggering of earthquakes as revealed from statistical analysis of global data. *Journal of Geophysical Research*, *107*(B10), ESE1-1–ESE1-11. https://doi.org/10.1029/2001jb001577

Thomas, A. M., Nadeau, R. M., & Bürgmann, R. (2009). Tremor-tide correlations and near-lithostatic pore pressure on the deep San Andreas fault. *Nature*, *462*(7276), 1048–1051. https://doi.org/10.1038/nature08654

van der Elst, N. J., Delorey, A. A., Shelly, D. R., & Johnson, P. A. (2016). Fortnightly modulation of San Andreas tremor and low-frequency earthquakes. *Proceedings of the National Academy of Sciences*, *113*(31), 8601–8605. https://doi.org/10.1073/pnas.1524316113

Wollin, C., Bohnhoff, M., Martínez-Garzón, P., Küperkoch, L., & Raub, C. (2018). A unified earthquake catalogue for the Sea of Marmara Region, Turkey, based on automatized phase picking and travel-time inversion: Seismotectonic implications. *Tectonophysics*, *747–748*, 416–444. https://doi.org/10.1016/j.tecto.2018.05.020

Yüce, H., & Alpar, B. (1997). Subtidal sea-level variations in the Sea of Marmara, their interactions with neighboring seas and relations to wind forcing. *Journal of Coastal Research*, *13*(4), 1086–1092.

Zaliapin, I., & Ben-Zion, Y. (2013). Earthquake clusters in southern California I: Identification and stability. *Journal of Geophysical Research: Solid Earth*, *118*(6), 2847–2864. https://doi.org/10.1002/jgrb.50179

Zhu, W., & Beroza, G. C. (2019). PhaseNet: A deep-neural-network-based seismic arrival-time picking method. *Geophysical Journal International*, *216*(1), 261–273. https://doi.org/10.1093/gji/ggy423

Zhu, W., McBrearty, I. W., Mousavi, S. M., Ellsworth, W. L., & Beroza, G. C. (2022). Earthquake phase association using a Bayesian Gaussian mixture model. *Journal of Geophysical Research: Solid Earth*, *127*(5), e2021JB023249. https://doi.org/10.1029/2021JB023249